Electrodynamics of planar Archimedean spiral resonator

N. Maleeva,[1,a)] A. Averkin,[1] N. N. Abramov,[1] M. V. Fistul,[1,2] A. Karpov,[1] A. P. Zhuravel,[3] and A. V. Ustinov[1,4]

[1]*Laboratory for Superconducting Metamaterials, National University of Science and Technology "MISIS,"*
Moscow 119049, Russia
[2]*Theoretische Physik III, Ruhr-Universitat Bochum, Bochum 44801, Germany*
[3]*B. Verkin Institute for Low Temperature Physics and Engineering, National Academy of Sciences of Ukraine,*
Kharkov 61103, Ukraine
[4]*Physikalisches Institut, Karlsruhe Institute of Technology (KIT), Karlsruhe 76131, Germany*

We present a theoretical and experimental study of electrodynamics of a planar spiral superconducting resonator of a finite length. The resonator is made in the form of a monofilar Archimedean spiral. By making use of a general model of inhomogeneous alternating current flowing along the resonator and specific boundary conditions on the surface of the strip, we obtain analytically the frequencies f_n of resonances which can be excited in such system. We also calculate corresponding inhomogeneous RF current distributions $\psi_n(r)$, where r is the coordinate across a spiral. We show that the resonant frequencies and current distributions are well described by simple relationships $f_n = f_1 n$ and $\psi_n(r) \simeq \sin[\pi n (r/R_e)^2]$, where $n = 1, 2 \ldots$ and R_e is the external radius of the spiral. Our analysis of electrodynamic properties of spiral resonators' is in good agreement with direct numerical simulations and measurements made using specifically designed magnetic probe and laser scanning microscope. © 2015 AIP Publishing LLC. [http://dx.doi.org/10.1063/1.4923305]

I. INTRODUCTION

Magic experiments of Nikola Tesla, which generated so much of excitement in the public of the *Belle Epoque*, had a solid base in research and patent activity. A spiral resonator appeared first in one of Tesla patents as early as 1897, as a tool for wireless RF power transfer.[1,2] Despite a wide use of the planar Archimedean spiral as antenna along the XX century,[3,4] a possibility to develop an analytical model of electrodynamics of a planar Archimedean spiral resonator and its inner resonance modes appeared to be elusive and was not fully explored. Our own attention to this topic is related to the development of metamaterials.[5]

Metamaterial is an artificially tailored media showing unusual electrodynamic properties. It is based on the use of compact magnetic and electric resonant elements, so-called meta-atoms.[6] The electrical and magnetic meta-atoms are sub-wavelength size micro-resonators that couple primarily to either electric or magnetic field of the incoming electromagnetic wave. At certain frequencies, close to resonances of both meta-atoms' types, the effective permeability and permittivity of such a media may become negative, resulting in effective negative index of refraction of the media. This effect is giving a multitude of opportunities for inventing non-trivial new optics, as pointed out in early theoretical work by Veselago[7] and more recent reviews.[8–10]

The first proposed magnetic meta-atoms were split-ring resonators.[5,11–13] The resonance frequency of such resonators is determined by the ratio between the width of the gap l and the size R of the ring, somewhat limiting the minimum ratio R/λ, where λ is the wavelength. The usage of planar spiral resonators was suggested in order to radically reduce the

resonator size relative to the wavelength.[14–16] Particularly, a spiral resonator behaves as a distributed resonator with multiple resonance modes, and couples primarily to the magnetic component of RF field perpendicular to spiral plane, in a way suitable for magnetic meta-atoms.

In this work, we develop an analytical model of Archimedean spiral resonator inner modes and verify it by experiments and detailed numerical simulations.

In a very simplified approach, the spiral resonator may be considered as straight-line resonator of a length L, rolled in a spiral (Fig. 1). This view leads to an assumption that the
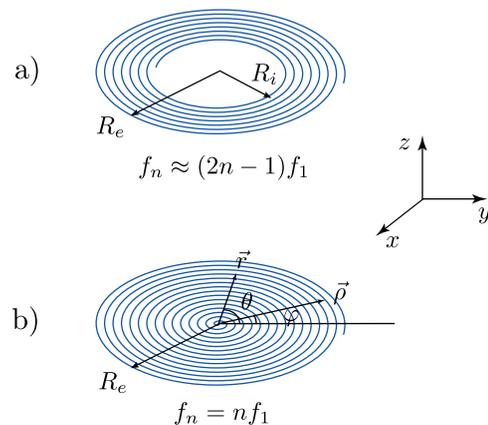
FIG. 1. (a) A sketch of monofilar planar ring-shaped spiral resonator, studied earlier in Ref. 17. Here, R_e is an external radius and $R_i \ll R_e$ is an internal radius of the spiral. The resonance frequencies of the ring-shaped spiral follow the sequence of the odd numbers as $f_1 : f_2 : f_3 : f_4 \ldots = 1 : 3 : 5 : 7 \ldots$. (b) A sketch of monofilar planar Archimedean spiral resonator considering in this work. Polar coordinates $\{\rho, \varphi\}$ and $\{r, \theta\}$ determine the coordinates of the point on the spiral and the observation point in the plane of the spiral, accordingly. Here, R_e is an external radius of the spiral. On the contrary to (a), the resonance frequencies of the Archimedean spiral follow the sequence of the integer numbers as $f_1 : f_2 : f_3 : f_4 \ldots = 1 : 2 : 3 : 4 \ldots$.

a)Electronic mail: maleeva@misis.ru.

spiral resonance frequencies are determined as the resonances in one-dimensional transmission line resonator with the length L with identical "open circuit" boundary conditions at both ends of transmission line

$$f_n = nf_1 = n\frac{c}{2L}, \tag{1}$$

where $n = 1, 2, 3...$ is the resonance number, c is the speed of light, and in our case $L \approx \pi R_e^2/d$, where R_e is the external radius of the spiral and d is the spiral period. The amplitude of a standing wave as a function of the distance l along the transmission line rolled in spiral, assuming the line to be uniform, is expected to be $I_n = I_0 \sin(n\pi \frac{l}{L})$. When the coordinate is expressed in terms of the radius r, the waveform at a resonance frequency is

$$I_n(r) = I_0 \sin\left(n\pi \left(\frac{r}{R_e}\right)^2\right). \tag{2}$$

While being simple and feasible, this approach, nevertheless, neglects the spiral geometry and interaction between the spiral turns.

The above simple model is not universal. For example, in contrast to Eq. (1), for a ring-shaped spiral resonator (Fig. 1(a)), the resonance frequencies expression turns out to be $f_n \approx (2n-1)f_1$.[17,18] Moreover, if the line is rolled in a ring-shaped spiral resonator,[17] the RF current amplitude distribution at resonance frequency is given by a more intricate expression than Eq. (2). From this point of view, it appears relevant to study in detail the resonance frequencies and the corresponding current distributions of a resonator formed by a planar Archimedean spiral (Fig. 1(b)).

In the following, we provide an analytical solution of Archimedean spiral resonator problem, obtaining both the resonance frequencies f_n and the corresponding current distributions in a resonator. We compare our analytical solution with the direct numerical simulation of electrodynamic properties of a spiral resonator excited by externally applied RF magnetic field. We present also an experimental study of microwave resonances of a single Archimedean spiral resonator by using both RF transmission measurements and two different spatially resolved probing techniques. From our experiments, we are able to extract the resonance frequencies and distributions of current and of the magnetic field near the spiral at these frequencies. Our experimental results firmly support the proposed electrodynamic model and analysis.

The paper is organized as follows. In Sec. II, we propose an analytical model of the planar Archimedean spiral resonator of a finite length and obtain the integro-differential equation determining the resonance frequencies f_n and the corresponding current distributions. We provide the approximate analytic solution of this equation, and calculate the resonance frequencies and current distributions. In Sec. III, we present an experimental study of planar Archimedean spiral resonators. The two different resonators were studied. The resonance frequencies are determined through the measurement of the frequency dependent transmission of an externally applied RF signal, i.e., $S_{21}(f)$. The experimental

current and the magnetic field distributions at the resonances were obtained by two methods: Laser Scanning Microscopy (LSM) for a resonator fabricated from superconducting Nb film and Magnetic Probe Scanning (MPS) for a resonator made of Cu. In Sec. IV, we present the direct numerical simulations of electrodynamic properties, in particular, the resonance frequencies and the current distributions in a spiral resonator exited by an externally applied microwave radiation. Section V contains conclusions.

II. ELECTRODYNAMICS OF A PLANAR SPIRAL RESONATOR

We consider the electrodynamics of a monofilar Archimedean spiral resonator of a finite length with N densely packed turns. In this case, the number of turns $N \gg 1$. The shape of the Archimedean spiral is described by equation written in polar coordinates as

$$\rho(\varphi) = R_e(1 - \alpha\varphi), \tag{3}$$

where φ is the polar angle, ρ is the polar radius varying from 0 to the external radius of the spiral R_e, and the parameter $\alpha = \frac{d}{2\pi R_e} = \frac{1}{2\pi N} \ll 1$, and d is the distance between adjacent turns. The schematic view of such a spiral resonator is shown in Fig. 1.

In order to obtain electrodynamic properties of a spiral resonator and, in particular, the resonance frequencies f_n, we use the method proposed in Refs. 19 and 20 for a resonator made in the form of a helical coil. A similar approach has been used also in Ref. 17 in order to describe electrodynamics of a ring-shaped spiral resonator. We assume that an alternating inhomogeneous current flows along the spiral. We also neglect current inhomogeneity inside of the spiral line. The coordinate and the time dependent radial and angular components of a vector-potential in cylindrical coordinates can be presented in the following form:[17]

$$A_r(t, z, r, \theta) = \frac{\mu_0 I e^{i\omega t}}{(4\pi)^2} \int_0^{R_e} d\rho \psi(\rho)$$
$$\times \int_0^\infty dx \frac{xe^{-\sqrt{x^2-k^2}|z|}}{\sqrt{x^2-k^2}} J_1[x\rho]J_1[xr] \tag{4}$$

and

$$A_\theta(t, z, r, \theta) = \frac{\mu_0 I e^{i\omega t}}{(4\pi)^2} \int_0^{R_e} d\rho \frac{\rho\psi(\rho)}{R_e\alpha}$$
$$\times \int_0^\infty dx \frac{xe^{-\sqrt{x^2-k^2}|z|}}{\sqrt{x^2-k^2}} J_1[x\rho]J_1[xr], \tag{5}$$

where I is the maximum value of the current excited in the spiral, $k = \omega/c$ is the wave vector, z is a coordinate perpendicular to the spiral plane, $\psi(\rho)$ describes normalized inhomogeneous current distribution across the spiral in the radial direction, and J_1 is the Bessel function of the first kind.[21]

In order to obtain the resonance frequencies f_n and the corresponding current distributions $\psi_n(\rho)$, we use a specific boundary condition, i.e., we require the component of an

electric field parallel to the strip surface to be equal to zero. This condition is written as

$$R_e \alpha E_r + r E_\theta|_{z=0} = 0. \tag{6}$$

The radial component E_r and the angular component E_θ of the electric field are expressed through corresponding components of the vector-potential as

$$E_r = \frac{1}{i\omega\epsilon_0\mu_0} \frac{d}{dr}\left[\frac{1}{r}\frac{d}{dr}(rA_r)\right] \tag{7}$$

and

$$E_\theta = -i\omega A_\theta. \tag{8}$$

Equations (4) and (5) can be simplified by using the following approximation: the wave vector k is much smaller than a typical inverse size of inhomogeneities in current distribution $\psi(\rho)$, i.e., $k \ll 1/R_e$.

With this approximation both components of the vector-potential in the plane of the spiral ($z = 0$) are written as follows:

$$A_r|_{z=0} = \frac{\mu_0 I e^{i\omega t}}{(4\pi)^2} \int_0^\infty dz \int_0^{R_e} d\rho\, \psi(\rho) \frac{1}{r^2}$$
$$\times \int_0^\infty dx\, e^{-\frac{zx}{r}} x J_1\left[\frac{\rho}{r}x\right] J_1[x] \tag{9}$$

and

$$A_\theta|_{z=0} = \frac{\mu_0 I e^{i\omega t}}{(4\pi)^2 R_e \alpha} \int_0^\infty dz \int_0^{R_e} d\rho\, \psi(\rho) \frac{\rho}{r^2}$$
$$\times \int_0^\infty dx\, x e^{-\frac{zx}{r}} J_1\left[\frac{\rho}{r}x\right] J_1[x]. \tag{10}$$

Introducing the new variables $\rho = R_e e^{-\tau}$ and $r = R_e e^{-\xi}$, the boundary condition (6) is written in the form of an integro-differential equation [see the details in the Appendix]

$$\int_0^\infty dz \int_0^\infty d\tau\, \psi(\tau)\Big(e^{3\xi} K_\xi''(\xi - \tau)$$
$$+ 2e^{3\xi} K_\xi'(\xi - \tau) + \frac{\omega^2 R_e^2}{c^2\alpha^2} e^{\xi-\tau} e^{-\xi} K(\xi - \tau) \Big) = 0, \tag{11}$$

where the kernel $K(\xi - \tau) = e^{-(\tau-\xi)} \int_0^\infty dx\, x e^{-\frac{zx}{r}} J_1[e^{-(\tau-\xi)}x] J_1[x]$. Since the kernel $K(\xi - \tau)$ resembles the δ-function, we apply a local approximation and obtain the differential equation for the current distribution $\psi(\xi)$

$$\int_0^\infty dz \Big[\psi'(0)e^{3\xi}K(\xi) + \int_{-\xi}^\infty du\, K(u)\Big(e^{3\xi}\psi_\xi''(\xi) + 2e^{3\xi}\psi_\xi'(\xi)$$
$$+ \frac{\omega^2 R_e^2}{c^2\alpha^2} e^{-u} e^{-\xi}\psi(\xi) \Big) \Big] = 0. \tag{12}$$

Here, we have taken into account that $\psi(\tau)|_{\tau=0,\infty} = 0$ and $K(\infty) = 0$.

Introducing a new variable $v = (r/R_e)^2 = e^{-2\xi}$ and explicitly calculating the integral over z, we obtain

$$-2\frac{K(v)}{g_1(v)}\psi_v'(1)v^{-2} + 4\psi_v''(v)$$
$$+ \frac{\omega^2 R_e^2}{c^2\alpha^2} \frac{g_2(v)}{g_1(v)}\psi(v) = 0. \tag{13}$$

Here, the expressions for the kernel $K(v)$, and functions $g_1(v)$ and $g_2(v)$ are written as $K(v) = R_e v \int_0^\infty dx J_1[v^{\frac{1}{2}}x]J_1[x]$, $g_1(v) = R_e v^{\frac{1}{2}} \int_{\sqrt{v}}^\infty du \int_0^\infty dx J_1[ux]J_1[x]$ and $g_2(v) = R_e v^{\frac{1}{2}} \int_{\sqrt{v}}^\infty du\, u^{-1} \int_0^\infty dx J_1[ux]J_1[x]$.

The solution of Eq. (13) can be obtained as following: First, we notice that with a good accuracy the ratio $\frac{g_2(v)}{g_1(v)}$ is equal to 1. At the next step, we consider a solution of the homogenous equation

$$\chi_v''(v) + \frac{\omega^2 R_e^2}{4c^2\alpha^2}\chi(v) = 0. \tag{14}$$

The solution of Eq. (14) is $\chi(v) = \sin(\frac{\omega R_e}{2c\alpha}v)$, where $v = r^2$, and therefore, we arrive on Eq. (2) obtained by qualitative analysis.

The eigenfunctions of Eq. (14) satisfying the boundary conditions are $\chi_n(v) = \sin(\pi n v)$. Thus, we search the solution of the inhomogeneous Eq. (13) in the following form:

$$\psi(v) = \sum_{n=1}^\infty A_n \sin \pi n v. \tag{15}$$

Substituting Eq. (15) into Eq. (13), we obtain

$$-2\pi\beta_n\left[\sum_{m=1}^\infty A_m m(-1)^m\right] - 2\pi^2 A_n n^2$$
$$+ \frac{\omega^2 R_e^2}{2c^2\alpha^2}A_n = 0, \tag{16}$$

where $\beta_n = \int_0^1 dv \frac{K(v)}{g_1(v)} v^{-2}\sin \pi n v$. The amplitude of n-th eigenfunction A_n is expressed in the following form:

$$A_n = \frac{2\pi\beta_n S}{-2\pi^2 n^2 + \frac{\omega^2 R_e^2}{2c^2\alpha^2}}. \tag{17}$$

Here, $S = \sum_{m=1}^\infty A_m m(-1)^m$. The amplitudes A_n were calculated for different resonant modes. The distributions of A_n for $n = 1...10$ are shown in Fig. 2. One can see that the main contribution in the form $\psi(v) = \sum_n A_n \sin \pi n v$ makes a summand coinciding with Eq. (2). The resonance frequencies of the spiral are determined by a transcendent equation

$$\pi = \sum_{m=1}^\infty \frac{(-1)^m m\beta_m}{-m^2 + \frac{\omega^2 R_e^2}{c^2\alpha^2}}. \tag{18}$$

Next, we numerically solve Eq. (18) and, therefore, obtain the resonance frequencies f_n for two spiral resonators: the first one (SR1) had dimensions $R_e = 16.25$ mm, $N = 23$, and $d = 0.7$ mm, and the second one (SR2) had dimensions $R_e = 1.5$ mm, $N = 75$, and $d = 0.02$ mm. In Table I (columns 3 and 6), the resonance frequencies f_n for ten modes
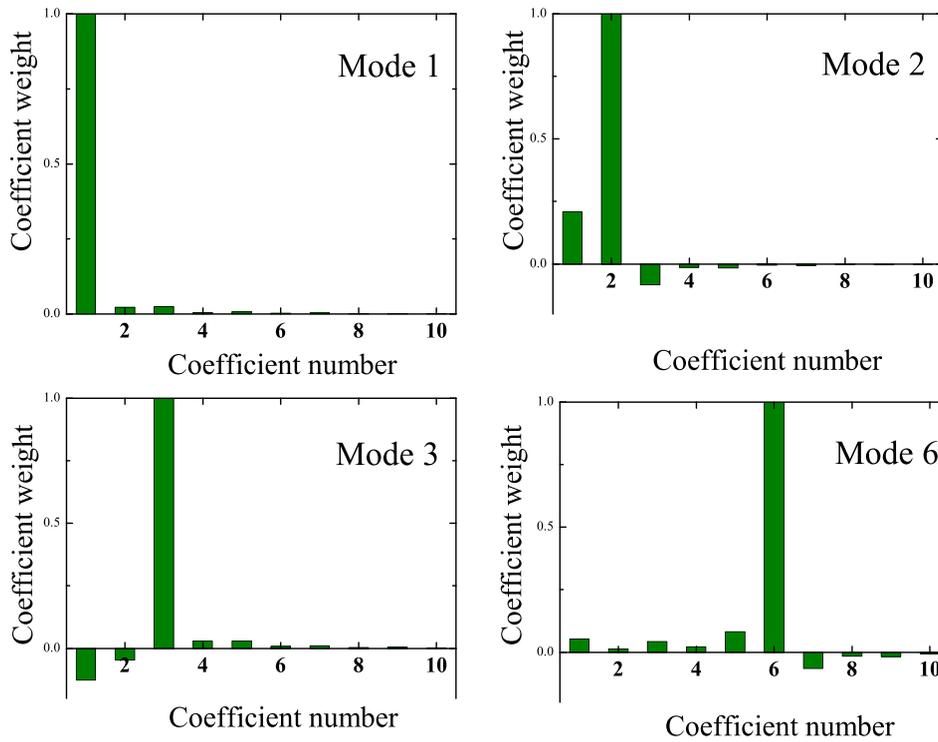
FIG. 2. Coefficients A_n of Eq. (15) analytically derived from Eq. (17) for the first, second, third, and sixth resonance modes (resonance frequencies). The coefficients A_n are normalized to the value of the maximal A_n for this particular mode. One can see that the main contribution to the current distribution is given by the coefficient with running number equals to the mode number. Thus, the most significant part of the standing wave profile can be explained by the solution of the simplified Eq. (14), amounting for about $90\% - 80\%$ of RF current at each mode.

$(n = 1...10)$ are presented. Note here that in experiment (see Sec. III) and in simulation (see Sec. IV), the spirals were placed at the substrate with dielectric constant ϵ_r. It is known that the effective dielectric constant for a structure at the interface of dielectric and air is approximately $\epsilon_{eff} = \frac{\epsilon_r + 1}{2}$. In order to compare analytical results with experiment and the simulation, we assume that the speed of light c appearing in Eq. (18) is reduced by the square root of the effective dielectric constant. The analytically obtained resonance frequencies are in a good agreement with experiments results. For SR1, the relative deviation is 13% for the first mode and 2%–4% for the higher modes. For SR2, the relative deviation is 8% for the first mode, 15% for the second mode, and 2%–7% for the higher modes. The deviation is related to details of the experimental setup, different for SR1 and SR2, not taken into account in the model. Moreover, the difference

in the resonance frequencies may be caused by the fact that the resonators used in the experiments are not as densely packed, as it was assumed in the model.

Using Eqs. (15) and (17), we obtain the RF current distributions in resonator SR2. These current distributions for four modes ($n = 1, 2, 3$, and 6) are presented in Fig. 3 (dotted lines). One can see a good agreement in locations of the minima and maxima and in the curve shape between experimental (solid lines) and high frequency structural simulator (HFSS) simulated (dashed lines) RF current profiles. In order to compare our analytical predictions with experiments carried out on resonator SR1, we calculated the magnetic field around the resonator. For this purpose, we approximate the spiral by the rings of variable radius a with the current distribution $\psi(a)$ (Eq. (15)). Thus, the radial component of magnetic field is[22]

TABLE I. Resonance frequencies of the SR1 and SR2 spiral resonators obtained experimentally, analytically, and from the simulations.

Mode number	Spiral resonator 1 resonance frequency			Spiral resonator 2 resonance frequency		
	Measured f_{Exp} (MHz)	Analytical f_{Anal}/f_{Exp}	HFSS simulated f_{HFSS}/f_{Exp}	Measured f_{Exp} (MHz)	Analytical f_{Anal}/f_{Exp}	HFSS simulated f_{HFSS}/f_{Exp}
1	80	0.87	1	128	1.08	1.14
2	180	0.96	0.99	299	1.15	1.03
3	268	0.92	0.99	465	1.05	1
4	353	0.97	0.99	635	1.07	0.99
5	437	0.97	0.99	801	1.04	0.99
6	522	0.98	0.99	971	1.05	0.99
7	607	0.97	0.99	1139	1.03	0.98
8	693	0.98	0.99	1307	1.04	0.98
9	779	0.97	0.99	1475	1.02	0.98
10	866	0.98	0.98	1643	1.03	0.98
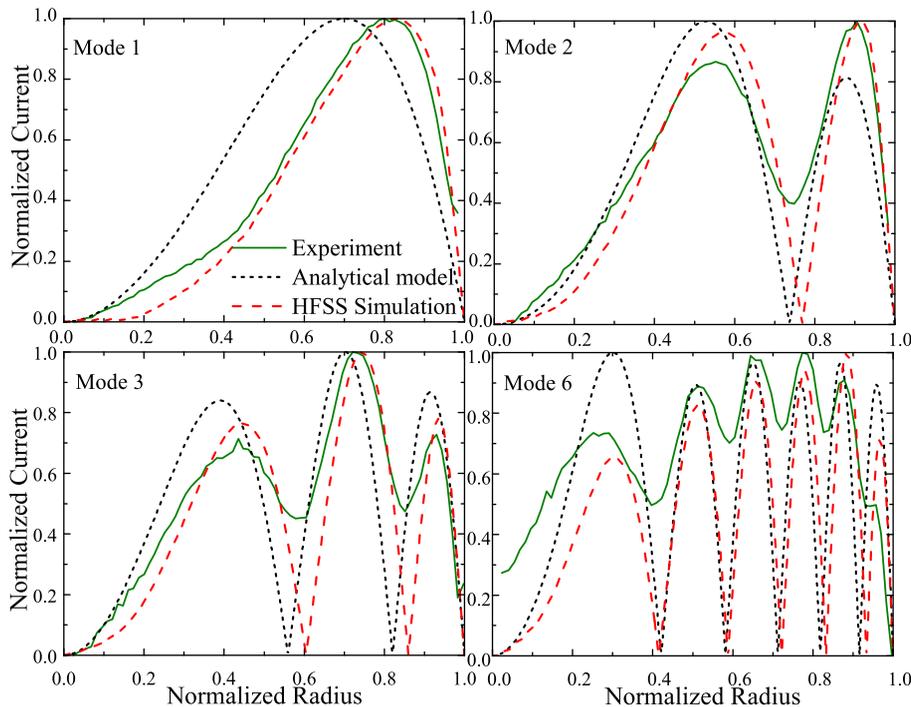
FIG. 3. Experimental and theoretical RF current distributions along the spiral radius for the first, second, third, and sixth inner resonance mode of a superconductive Nb spiral (SR2). The data are measured with LSM (solid line). Although smoothed by the thermal dissipation in the substrate, experimental data are visibly in a good agreement with analytical model (dotted line) and HFSS simulation (dashed line). The spiral dimensions are $R_e = 1.5$ mm, $N = 75$, $d = 0.02$ mm, and the substrate is 0.35 mm thick Si.

$$B_r(r,z) = \int_0^{R_e} da \frac{\psi(a)}{c} \frac{2z}{r\sqrt{(a+r)^2+z^2}}$$

$$\times \left[-K\left(\frac{\sqrt{4ar}}{\sqrt{(a+r)^2+z^2}} \right) \right.$$

$$\left. + \frac{a^2+r^2+z^2}{(a-r)^2+z^2} E\left(\frac{\sqrt{4ar}}{\sqrt{(a+r)^2+z^2}} \right) \right], \quad (19)$$

where $K\left(\frac{2r}{\sqrt{4r^2+z^2}} \right)$ and $E\left(\frac{2r}{\sqrt{4r^2+z^2}} \right)$ are complete elliptic integrals of the first and second kind. Using the corresponding $\psi(r)$ distribution, the radial component of magnetic field for the copper resonator (SR1) is calculated and is presented in Fig. 4 (dotted lines), also for all four modes. The magnetic field is calculated at the distance of $z = 0.3$ mm from the plane of the resonator, corresponding to the setting of the probe loop used in experimental setup. The analytically obtained results are in a good agreement with the measured (solid lines) and with the HFSS predicted (dashed lines) mode profiles in terms of the locations of minima and maxima, and of the curves shape (Fig. 4).

III. EXPERIMENT

Our electrodynamic analytical model of the resonance modes of a spiral resonator has been verified through the direct measurement of resonance frequencies, the local RF currents, and the RF magnetic fields of the spiral resonators. First, spiral resonator (SR1) is fabricated as copper printed circuit board (PCB) on a hydrocarbon ceramic laminate substrate (RO4350B) with dielectric constant $\epsilon_r = 3.48$ and thickness 0.765 mm. The copper trace width is 0.3 mm. The second resonator (SR2) is made from superconducting Nb

thin film. SR2 is fabricated by lift-off photolithography on a Si substrate with dielectric constant $\epsilon_r = 11.45$ at 4 K temperature.[23] The width of the Nb trace is 10 μm and the gap between the adjacent turns is 10 μm wide.

The resonance frequencies of the both spiral resonators SR1 and SR2 are detected in RF transmission measurements in a way similar to Ref. 18 and the results are presented in Table I. The two different experimental techniques are used to study the electrodynamic properties of resonators. The SR1 is studied by specifically designed MPS allowing one to measure the RF magnetic field distribution around the resonator. At the same time, the superconducting resonator SR2 is studied with LSM, allowing one to obtain directly the RF current distribution across the spiral.

The radial component of the magnetic field near the surface of the SR1 is measured with MPS at room temperature using a small loop antenna as a probe. A sketch of the MPS experimental setup is shown in Fig. 5(a). Here, in order to excite the resonator, a 32 mm diameter shielded excitation loop is used as an RF field source. The loop is made of the 2 mm semi-rigid 50 Ω coaxial cable and is positioned at 30 mm below the spiral resonator, far enough to ensure the weak coupling.

The radial component of the RF magnetic field near the surface of SR1 resonator is measured with loop antenna of about 0.5 mm in diameter formed at the end of 0.5 mm diameter semi-rigid 50 Ω coaxial cable. This probe is placed at a distance of about 50 μm from the surface of the spiral and its plane is oriented perpendicular to the radius of the spiral. Thus, the full distance from the center of the probe loop to the surface of the spiral is about 0.3 mm. A motorized linear motion actuator is used to move the probe loop along the radius of the spiral and thus to measure the magnetic field spatial distribution. The movement step is 0.135 mm, small enough to resolve the RF magnetic field (current distribution)
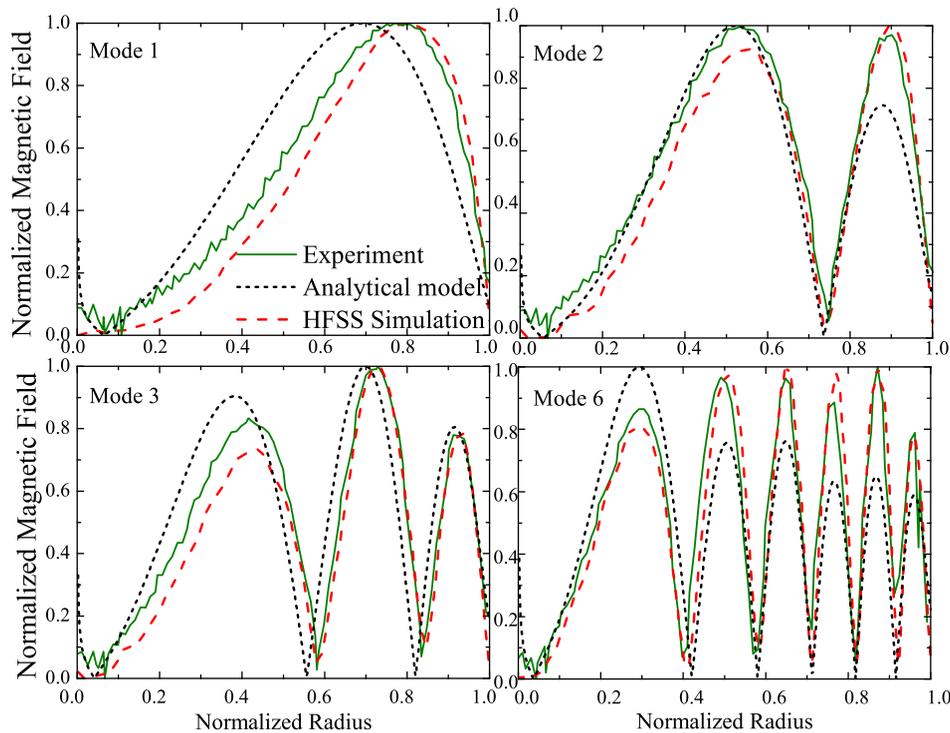
FIG. 4. Experimental (solid line), theoretical (dotted line), and numerically simulated (dashed line) amplitudes of the RF magnetic field versus radial coordinate of the spiral. The data are the normalized radial component of the magnetic field for the first, second, third, and sixth modes of copper spiral resonator (SR1). The radial component of RF magnetic field is measured with a network analyser via a mobile probing loop (as in Fig. 5). The loop diameter is smaller than the spiral step and its plane is perpendicular to the radius, providing sensitivity to a radial component of the RF magnetic field. Also, the distance from the probing loop to the spiral surface is small (0.3 mm) in comparison with the spiral line width. Naturally, in the vicinity of the surface the radial component of the RF magnetic field profile is very similar to the profile of the RF current. The dotted line corresponds to the analytically obtained function $B_r(r,z)$ with $z = 0.3$ mm of the perfect conductor spiral. The dashed line corresponds to the radial component of the magnetic field obtained by the HFSS simulation of the superconductive spiral on the substrate. Simulated magnetic field is taken at $z = 0.3$ mm as well. The SR1 has 23 turns with the period $d = 0.7$ mm and with external radius $R_e = 16.25$ mm.

of the individual turns. Excitation signal is generated and probe signal is measured using a vector network analyzer. Both the motorized drive and the network analyser are controlled by PC. In our experimental setup, the S_{21} transmission coefficient is proportional to the amplitude of RF voltage generated in the probe loop (while the excitation amplitude is

FIG. 5. Experimental setup for detecting the profile of the standing wave of the inner modes of a spiral resonator. (a) The sketch for RF MPS measurement. The probe loop is oriented perpendicular to the radius of the spiral to sense mostly the radial component of the RF magnetic field. The arrowed line represents trajectory (radius) along witch the probe loop can be moved by the motorized drive. (b) The sketch for laser scanning measurement. The laser beam is scanned over the superconducting spiral and perturbs the superconducting state in small area of the resonator. The enhanced concentration of normal electrons (quasiparticles) leads to a change of the transmission of the RF signal through resonator. The induced variation of the transmission coefficient S_{21} corresponds to the squared amplitude of local RF current in the probed area of the circuit.[24]

constant), and thus proportional to the local amplitude of the magnetic flux.

The measured spatial distributions of the radial component of the RF magnetic field for four modes ($n = 1, 2, 3$, and 6) are presented in Fig. 4 (solid lines). For each mode, the curves are obtained by combining measurements along four orthogonal radial directions, allowing for complementing the data.

A low-temperature LSM[24] is used to examine in-plane x–y distribution of RF microwave currents in superconducting resonator SR2. A number of specific schemes for the LSM electronics designed for the different detection modes have been published elsewhere[25–28] and it is not a subject of discussion here. The LSM uses the principle of the point-by-point x–y scanning of the superconducting planar structure by a sharply focused laser beam (see Fig. 5(b)). Here, we use a setup that is specially designed for imaging of current distribution in superconducting RF samples with in-plane dimensions up to 10×10 mm. Our LSM spatial resolution is limited by the capabilities of objective lens focusing optical beam to about 5 μm. The focused beam acts as a local heat source in any point of the optical raster in the plane of the studied device. The power of the laser beam is set to about 10 nW (at 670 nm light wavelength). The induced perturbation is low enough not to change significantly the RF current distribution, while keeping LSM photo-response (PR) detectable. The intensity of the laser light is modulated

in amplitude at the typical frequency of about $f_m \sim 100$ kHz in order to increase the signal-to-noise ratio by using a lock-in detection technique. The modulation helps reducing the size of the thermal perturbation area proportional to $1/\sqrt{f_m}$ down to 20 μm at 100 kHz modulation.[24]

The laser scanning microscope images of the first, second, third, and sixth mode standing wave patterns of Nb superconducting resonator SR2 are presented in Figs. 6(a)–6(d), respectively. The grey scale corresponds to the amplitude of photo response and can be interpreted as the squared amplitude of RF current flowing locally in the spiral (bright is large and dark is small RF current). The outer border of the spiral structure is given by the dashed line. One can see from Fig. 6(a) that in the fundamental mode, there is the only one light-colored circle inside the resonator limits. The RF currents are lager in the middle part of the Nb resonator, and decay towards both ends of the spiral line. For the second mode (Fig. 6(b)), there are two rings of strong currents. Higher harmonics (Figs. 6(c) and 6(d)) demonstrate a proportional increase in number of bright circles corresponding to local peaks in RF current. This confirms that the spiral acts as a distributed resonator with integer number of half-wavelengths of current at each eigenmode. The cross-sectional radial profiles of standing waves are extracted from the images and are plotted by solid lines in Fig. 3. One can note that all the profiles are smoothed off and, as a result, the measured current is not reaching zero at the RF current nodes. This can be explained by the smearing effect of the thermal spot, produced by laser beam when illuminating the Si substrate of the Nb resonator. The absorption coefficient

in Si at 670 nm light wavelength is of about 65%, and the calculated size of the thermal spot in Si substrate is larger than 20 μm (for T = 4 K and f_m = 100 kHz). Thus, by extra heating through the substrate the laser beam generates additional LSM PR over 2–3 adjacent turns of Nb spiral. Note that this experimental artifact does not affect the measured locations of the RF current nodes and antinodes.

IV. SIMULATION

In order to verify the developed analytical model and to validate the experimental data, we use the ANSYS HFSS.[29] The driven mode HFSS program is used for calculating the resonance frequencies and the shape of the standing waves of the resonant modes in both spirals used in our experiments. In HFSS calculations, the planar spirals are assumed to be made of infinitely thin lossless metal layer situated at the substrate with appropriate dielectric permittivity ϵ_r. The HFSS simulated circuit structure follows the experimental setup from Fig. 5(b), where the spiral resonator sample is placed in between of the two weakly coupled magnetic loops. In order to ensure a weak coupling of the two loops, the inter-loop distance is set at four loop radii ($4R_e$). Also in HFSS model, the two circuit terminals are inserted it a break in each of the coupling loops, and the resonance frequencies are determined from simulated terminal 1 to terminal 2 transmission (S_{21}) data.

The HFSS calculated resonance frequencies of SR1 are in a perfect agreement with experiment, remaining within 1% of relative deviation for the first 10 resonant modes (Table I, column 4). Next, we simulate with HFSS the waveform of the standing wave of RF magnetic field for four resonance modes (n = 1, 2, 3, and 6) of spiral resonator SR1, as measured in experiment of Fig. 5(a). At the resonance frequencies, we calculated the radial component of RF magnetic field along the radial line running from the spiral center, at a constant distance of 0.3 mm from the spiral surface (as in experiment Fig. 5(a)). In this experiment, the radial component of RF magnetic field is measured with a miniature loop probe at the same distance (solid line in Fig. 4). The HFSS calculated radial magnetic RF field component is plotted as well in Fig. 4 as a dashed line. The measured (solid line) and the HFSS predicted (dashed line) mode profiles are in a very good agreement in terms of the locations of minima and maxima along the radial axis, of the amplitude of the maxima, as well as in the curve shapes (Fig. 4). The analytical prediction has a similar precision, of about 3% in resonance frequency, but requires a lower volume of calculations (Table I, column 3).

For the resonator SR2 made of superconducting Nb, the HFSS simulated resonance frequencies are listed in Table I, column 7. The precision of the HFSS prediction is very good, within 2% of the measured values, except for the first resonant mode, where the deviation is 14%. The deviation of the first mode resonance frequency may be related to the details of experimental setup, such as the metal parts of the cryogenic equipment, not taken into account in HFSS calculations. Next, we calculated with HFSS the waveform of the standing wave of RF current for four resonance modes

FIG. 6. The measured standing wave patterns of RF current for the first, second, third, and the sixth inner modes of Nb superconducting spiral resonator (SR2). The images are obtained with cryogenic LSM. Higher level of RF current is given in a lighter grey scale; the edge of Nb spiral is marked by a dashed line. The frequencies of the resonances in resonator SR2 are listed in Table I. Note a smearing effect of the light absorption in the spiral substrate, giving a halo outside of the spiral structure. The extracted radial profiles of the RF current of the modes are also smeared, see Fig. 3.

(n = 1, 2, 3, and 6) of spiral resonator SR2. The value of the RF current in the spiral section is calculated applying Stoke's theorem (or Ampere's circuital law), as a line integral of the magnetic field around closed curve, encircling a section of conductive line of the spiral. This approach gave the best precision in calculation of the RF current, and is applied to 1800 points along the spiral resonator 2. The HFSS calculated profiles of RF current for the different modes in SR2 are given in Fig. 3 as dashed lines. In Fig. 3, one can note a very good mutual agreement in locations of the minima and maxima of experimental (solid line) and HFSS simulated (dashed line). The analytical prediction is giving a similar precision for the resonance frequencies, of about 4%, except 15% deviation at the second mode (Table I, column 6).

V. CONCLUSION

We developed an analytical model describing electrodynamics of a planar monofilar Archimedean spiral resonator of a finite length and verified it numerically and experimentally. We analytically obtain the resonance frequencies and corresponding RF current distributions in spiral resonator. In contrast to previously studied ring-shaped spiral resonator,[15,17] the Archimedean spiral's set of resonance frequencies derived from our model is $f_n = f_1 n$, where $n = 1, 2...$, which is similar to resonances of a straight-line resonator with open ends. Thus, the distribution of resonant frequencies depends crucially on the details of the geometry of the spiral.

Next, our analytic solutions are compared with experiment and direct numerical simulations. Experimental and simulated resonance frequencies follow the predicted relationship, $f_n = f_1 n$, in agreement with analytical model (see Table I). The difference between analytical and measured, or simulated results significantly decreases with increasing of the mode number. This can be due to the fact that, for lower modes, the electric and magnetic fields are wider spread in space than for upper modes. A widely spread RF field of lower modes interacts with surrounding parts of experimental setup, thus perturbing the spiral resonator eigenmodes and shifting their frequencies. The shape of the standing waves predicted by analytical model is in a good agreement with simulations and experiments (Figs. 3 and 4). The difference in positions of maxima and minima could be explained by the fact that the resonators used in experiment and in simulation are not as densely packed as they are assumed in the model.

To summarize, we have studied theoretically (analytical calculations and numerical simulations) and experimentally the electrodynamic properties of the planar Archimedean spiral resonators of a finite length. By making use of a model of inhomogeneous alternating current flowing along the spiral resonator and of specific boundary conditions (see, Eq. (6)), we derived an integro-differential equation (11) which, in turn, determines the resonance frequencies and the corresponding RF current distributions in the spiral. Next, by applying a local approximation, we solved Eq. (11) and obtained the resonance frequencies and the corresponding current distributions of the Archimedean spiral resonator. A good quantitative agreement is found between the analysis,

direct numerical simulations, and experiments performed with two spiral resonators made of different materials.

Our analysis of electrodynamic properties of a single spiral resonator can be useful for metamaterials design. Indeed, the metamaterials containing the 3D or 2D arrays of such resonators may show negative permeability,[11] when the frequency of incoming microwave radiation is close to resonant frequency. Also, the usage of superconducting spiral resonators may allow one to greatly reduce the RF dissipation effects. Moreover, obtained, here, resonance frequencies f_n determine the frequency bands, in which the real part of the metamaterial permeability may be negative, and the current distribution functions inside of the spiral determine the spirals interaction in the metamaterial. Our results also may find application in development of short range wireless power transfer (WPT) systems.[30–34]

APPENDIX: CALCULATION DETAILS

In this appendix, we present intermediate steps allowing one to obtain the integro-differential equation (11). We use the following approximation: the wave vector k is much smaller than a typical inverse size of inhomogeneities in current distribution $\psi(\rho)$, i.e., $k \ll 1/(R_e - R_i)$. Moreover, we consider a wide planar spiral, i.e., $R_i \simeq 0$. With these approximations, we have rewritten Eqs. (4) and (5) as

$$A_r = \frac{\mu_0 I e^{i\omega t}}{(4\pi)^2} \int_0^{R_e} d\rho\,\psi(\rho) \int_0^{\infty} dx\, e^{-zx} J_1[\rho x] J_1[rx] \tag{A1}$$

and

$$A_\theta = \frac{\mu_0 I e^{i\omega t}}{(4\pi)^2 R_e \alpha} \int_0^{R_e} d\rho\,\psi(\rho)\rho \int_0^{\infty} dx\, e^{-zx} J_1[\rho x] J_1[rx]. \tag{A2}$$

In order to obtain components of the vector potential in the plane of the spiral ($z = 0$) let's use such an identity: $A_r|_{z=0} = -\int_0^{\infty} dz \frac{\partial}{\partial z} A_r$

$$A_r|_{z=0} = \frac{\mu_0 I e^{i\omega t}}{(4\pi)^2} \int_0^{\infty} dz \int_0^{R_e} d\rho\,\psi(\rho) \frac{1}{r^2}$$
$$\times \int_0^{\infty} dx\, x e^{-\frac{zx}{r}} J_1\left[\frac{\rho}{r} x\right] J_1[x] \tag{A3}$$

and

$$A_\theta|_{z=0} = \frac{\mu_0 I e^{i\omega t}}{(4\pi)^2 R_e \alpha} \int_0^{\infty} dz \int_0^{R_e} d\rho\,\psi(\rho) \frac{\rho}{r^2}$$
$$\times \int_0^{\infty} dx\, x e^{-\frac{zx}{r}} J_1\left[\frac{\rho}{r} x\right] J_1[x]. \tag{A4}$$

Let us designate $\rho = R_e e^{-\tau}$ and $r = R_e e^{-\xi}$. Thus,

$$A_r = \frac{\mu_0 I e^{i\omega t}}{(4\pi)^2 R_e} \int_0^\infty dz \int_0^\infty d\tau \psi(\tau) e^\tau e^{-2(\tau-\xi)}$$
$$\times \int_0^\infty dx\, x e^{-\frac{zx}{r}} J_1\left[e^{-(\tau-\xi)}x\right] J_1[x] \quad \text{(A5)}$$

and

$$A_\theta = \frac{\mu_0 I e^{i\omega t}}{(4\pi)^2 R_e \alpha} \int_0^\infty dz \int_0^\infty d\tau \psi(\tau) e^{-2(\tau-\xi)}$$
$$\times \int_0^\infty dx\, x e^{-\frac{zx}{r}} J_1\left[e^{-(\tau-\xi)}x\right] J_1[x]. \quad \text{(A6)}$$

Next, we identify a kernel $K(\xi - \tau)$ as

$$K(\xi - \tau) = e^{-(\tau-\xi)} \int_0^\infty dx\, x e^{-\frac{zx}{r}} J_1\left[e^{-(\tau-\xi)}x\right] J_1[x]. \quad \text{(A7)}$$

Using Eq. (A7), the components of the vector potential are expressed as follows:

$$A_r = \frac{\mu_0 I e^{i\omega t}}{(4\pi)^2 R_e} \int_0^\infty dz \int_0^\infty d\tau \psi(\tau) e^\xi K(\xi - \tau) \quad \text{(A8)}$$

and

$$A_\theta = \frac{\mu_0 I e^{i\omega t}}{(4\pi)^2 R_e \alpha} \int_0^\infty dz \int_0^\infty d\tau \psi(\tau) e^{\xi-\tau} K(\xi - \tau). \quad \text{(A9)}$$

Let us write the components of the electric field, i.e., the angular component E_θ

$$E_\theta = -\frac{i\omega \mu_0 I e^{i\omega t}}{(4\pi)^2 R_e \alpha} \int_0^\infty dz \int_0^\infty d\tau \psi(\tau) e^{\xi-\tau} K(\xi - \tau) \quad \text{(A10)}$$

and

$$E_r = \frac{1}{i\omega \epsilon_0 \mu_0} \left(-\frac{1}{R_e} e^\xi \frac{d}{d\xi} \left[-\frac{1}{R_e^2} e^{2\xi} \frac{d}{d\xi} \left(R_e e^{-\xi} A_r \right) \right] \right). \quad \text{(A11)}$$

Here, we have taken into account that $r = R_e e^{-\xi}$ and $\frac{d}{dr} = -\frac{1}{R_e} e^\xi \frac{d}{d\xi}$.

Using Eq. (A7), the radial component of the electric field E_r is written as

$$E_r = \frac{I e^{i\omega t}}{i\omega \epsilon_0 (4\pi)^2 R_e^3} \int_0^\infty dz \int_0^\infty d\tau \psi(\tau) e^{3\xi}$$
$$\times \left(K_\xi''(\xi - \tau) + 2K_\xi'(\xi - \tau) \right). \quad \text{(A12)}$$

Finally, Eq. (6) is written as

$$\int_0^\infty dz \int_0^\infty d\tau \psi(\tau) (e^{3\xi} K_\xi''(\xi - \tau)$$
$$+ 2e^{3\xi} K_\xi'(\xi - \tau) + \frac{\omega^2 R_e^2}{c^2 \alpha^2} e^{\xi-\tau} e^{-\xi} K(\xi - \tau)) = 0. \quad \text{(A13)}$$

[1]N. Tesla, U.S. patent 645,576 (20 March 1900).
[2]N. Tesla, *My Inventions* (Electrical Experimenter, 1919).
[3]L. Schneider, X. Begaud, M. Soiron, B. Perpere, and C. Renard, IET Microwave Antennas Propag. **1**(1), 212–216 (2007).
[4]H. Nakano, R. Satake, and J. Yamauchi, IEEE Trans. Antennas Propag. **58**(5), 1511 (2010).
[5]M. Ricci, N. Orloff, and S. M. Anlage, Appl. Phys. Lett. **87**, 034102 (2005).
[6]N. Engheta and R. W. Ziolkowski, *Metamaterials: Physics and Engineering Explorations* (Wiley and Sons, New York, 2006); S. Zouhdi, A. Sihvola, and Al. P. Vinogradov, *Metamaterials and Plasmonics: Fundamentals, Modelling, Applications* (Springer-Verlag, New York, 2008).
[7]V. G. Veselago, Usp. Fiz. Nauk **92**, 517 (1967) [Sov. Phys. Usp. **10**, 509 (1968)].
[8]J. B. Pendry, Phys. Rev. Lett. **85**, 3966 (2000).
[9]N. I. Zheludev, Science **328**, 582 (2010).
[10]P. Jung, A. V. Ustinov, and S. M. Anlage, Supercond. Sci. Technol. **27**, 073001 (2014).
[11]J. B. Pendry, A. J. Holden, D. J. Robbins, and W. J. Stewart, IEEE Trans. Microwave Theory Tech. **47**, 2075 (1999).
[12]R. A. Shelby, D. R. Smith, S. C. Nemat-Nasser, and S. Schultz, Appl. Phys. Lett. **78**, 489 (2001); R. A. Shelby, D. R. Smith, and S. Schultz, Science **292**, 77 (2001).
[13]M. C. Ricci and S. M. Anlage, Appl. Phys. Lett. **88**, 264102 (2006).
[14]J. D. Baena, R. Marques, F. Medina, and J. Martel, Phys. Rev. B **69**, 014402 (2004).
[15]C. Kurter, J. Abrahams, and S. M. Anlage, Appl. Phys. Lett. **96**, 253504 (2010).
[16]S. Massaoudi and I. Huynen, Microwave Opt. Technol. Lett. **50**, 1945 (2008).
[17]N. Maleeva, M. V. Fistul, A. Karpov, A. P. Zhuravel, A. Averkin, P. Jung, and A. V. Ustinov, J. Appl. Phys. **115**, 064910 (2014).
[18]C. Kurter, A. P. Zhuravel, J. Abrahams, C. L. Bennett, A. V. Ustinov, and S. M. Anlage, IEEE Trans. Appl. Supercond. **21**, 709 (2011).
[19]S. Kh. Kogan, Dokl. Akad. Nauk. **66**, 867 (1949) (in Russian).
[20]R. A. Silin and V. P. Sazonov, *Zamedlyaushie Sistemi* (Soviet Radio, Moscow, 1966) (in Russian).
[21]M. Abramovitz and I. A. Stegun, *Handbook of Mathematical Functions with Formulas, Graphs, and Mathematical Tables* (Dover Publications, New York, 1972).
[22]L. D. Landau, E. M. Lifshitz, and L. P. Pitaevskii, *Electrodynamics of Continuous Media* (Butterworth-Heinemann, 1984).
[23]J. Krupka, J. Breeze, A. Centeno, N. Alford, T. Claussen, and L. Jensen, IEEE Trans. Microwave Theory Tech. **54**, 3995–4001 (2006).
[24]A. P. Zhuravel, S. M. Anlage, and A. V. Ustinov, IEEE Trans. Appl. Supercond. **17**(2), 902–905 (2007).
[25]A. P. Zhuravel, A. G. Sivakov, O. G. Turutanov, A. N. Omelyanchouk, S. M. Anlage, A. Lukashenko, A. V. Ustinov, and D. Abraimov, Low Temp. Phys. **32**, 592–607 (2006).
[26]A. P. Zhuravel, S. M. Anlage, and A. V. Ustinov, J. Supercond. Novel Magn. **19**(7–8), 625–632 (2006).
[27]A. P. Zhuravel, S. M. Anlage, and A. V. Ustinov, Appl. Phys. Lett. **88**, 212503 (2006).
[28]A. G. Sivakov, A. P. Zhuravel, O. G. Turutanov, and I. M. Dmitrenko, Appl. Surf. Sci. **106**, 390–395 (1996).
[29]See www.ansys.com for ANSYS HFSS.
[30]A. Kurs, A. Karalis, R. Moffatt, J. D. Joannopoulos, P. Fisher, and M. Soljacic, Science **317**, 83 (2007).
[31]E. Waffenschmidt, in Proceedings of VDE-Kongress 2010, Magdeburg, 2010.
[32]W. C. Brown, IEEE Trans. Microwave Theory Tech. **32**, 1230 (1984).
[33]A. Karalis, J. D. Joannopoulos, and M. Soljacic, Ann. Phys. **323**(1), 34–48 (2008).
[34]T. Beh, M. Kato, T. Imura, and Y. Hori, World Electric Vehicle J. **4**, 744–753 (2010).